




Title	Vertical fine structure and time evolution of plasma irregularities in the Es layer observed by a high-resolution Ca <sup>+</sup> lidar
Authors	Ejiri Mitsumu K., Nakamura Takuji, Tsuda Takuo T., Nishiyama Takanori, Abo Makoto, Takahashi Toru, Tsuno Katsuhiko, Kawahara Takuya D., Ogawa Takayo, Wada Satoshi
Citation	Earth, Planets and Space, 71(3), 1-10, 2019
Issue Date	2019-1-11
Type	Journal Article
URL	<a href="https://doi.org/10.1186/s40623-019-0984-z">https://doi.org/10.1186/s40623-019-0984-z</a>
Right	
Textversion	publisher

FULL PAPER

Open Access



# Vertical fine structure and time evolution of plasma irregularities in the $E_s$ layer observed by a high-resolution $\text{Ca}^+$ lidar

Mitsumu K. Ejiri<sup>1,2\*</sup> , Takuji Nakamura<sup>1,2</sup>, Takuo T. Tsuda<sup>3</sup>, Takanori Nishiyama<sup>1,2</sup>, Makoto Abo<sup>4</sup>, Toru Takahashi<sup>1</sup>, Katsuhiko Tsuno<sup>5</sup>, Takuya D. Kawahara<sup>6</sup>, Takayo Ogawa<sup>5</sup> and Satoshi Wada<sup>5</sup>

## Abstract

The vertical fine structures and the time evolution of plasma irregularities in the sporadic  $E$  ( $E_s$ ) layer were observed via calcium ion ( $\text{Ca}^+$ ) density measurements using a resonance scattering lidar with a high time-height resolution (5 s and 15 m) at Tachikawa (35.7°N, 139.4°E) on December 24, 2014. The observation successfully provided clearer fine structures of plasma irregularities, such as quasi-sinusoidal height variation, localized clumps, “cats-eye” structures, and twist structures, in the sporadic  $\text{Ca}^+$  ( $\text{Ca}^+_s$ ) layers at around 100 km altitude. These fine structures suggested that the Kelvin–Helmholtz instabilities occurred in the neutral atmosphere whose density changed temporarily or spatially. The maximum  $\text{Ca}^+$  density in the  $\text{Ca}^+_s$  layer was two orders of magnitude smaller than the maximum electron density estimated from the critical frequency ( $f_oE_s$ ) simultaneously observed by the ionosonde at Kokubunji (35.7°N, 139.5°E). A strong positive correlation with a coefficient of 0.91 suggests that  $\text{Ca}^+$  contributes forming the  $E_s$  layer as well as major metallic ions  $\text{Fe}^+$  and  $\text{Mg}^+$  in the lower thermosphere. Moreover, the formation of a new  $\text{Ca}^+_s$  layer at 110 km and the upward motions of the  $\text{Ca}^+_s$  layers at 100 km and 110 km were observed before the local sunrise and just after the sunrise time at the conjugation point. Although the presence or absence of a causal relationship with the sunrise time was not clear, a possible explanation for the formation and the upward motions of the  $\text{Ca}^+_s$  layers was the occurrence of strong horizontal wind, rather than the enhancement of the eastward electric field.

**Keywords:** Sporadic  $E$  ( $E_s$ ) layer, Calcium ion ( $\text{Ca}^+$ ) density, Resonance scattering lidar, Mid-latitude, Vertical fine structure, Kelvin–Helmholtz instability, Ion upward flow, Lower thermosphere

## Introduction

The sporadic  $E$  ( $E_s$ ) layer is a thin layer, typically 2–10 km in height, with a high electron density observed between 90 and 130 km. Formation mechanisms of the  $E_s$  layer have been studied since the 1960s (e.g., MacLeod 1966; Whitehead 1961, 1970, 1989). One of the theories of the formation mechanisms for  $E_s$  layer is the wind shear theory that ions are converged in a thin layer by vertical shear of horizontal neutral wind in the lower thermosphere in the mid-latitude (Whitehead 1989; Mathews 1998; Haldoupis 2012). The primary ionic species for

the  $E_s$  layer formation are metallic (e.g.,  $\text{Fe}^+$ ,  $\text{Mg}^+$ ,  $\text{Na}^+$ ,  $\text{Ca}^+$ ), originating from meteors. These metallic ions have a longer lifetime than the dominant species ( $\text{O}^+$ ,  $\text{NO}^+$ ,  $\text{O}_2^+$ ) in the ionospheric  $E$ -region. Simultaneous observations of electron density and metallic  $\text{Ca}^+$  ion density in the  $E_s$  layer using the incoherent scatter (IS) radar and a resonance scattering lidar, respectively, at the Arecibo Radio Observatory (18.4°N, 66.8°W) showed that the  $\text{Ca}^+$  densities were directly related to the strength of the  $E_s$  layer (Raizada et al. 2012).

Radio and optical measurements such as radars and satellite imaging, have revealed that electron densities in the  $E_s$  layers are not uniform or constant but have irregular structures in time and space. VHF radars, including the middle and upper atmosphere (MU) radar, have observed quasi-periodic (QP) echoes, which

\*Correspondence: ejiri.mitsumu@nipr.ac.jp

<sup>1</sup> National Institute of Polar Research, 10-3, Midoricho, Tachikawa, Tokyo 190-8518, Japan

Full list of author information is available at the end of the article

indicate significant perturbations in time and height in the  $E_s$  layer (Yamamoto et al. 1991, 1992). Ionosonde observations also found the existence of irregular structures by large differences between the critical ( $f_oE_s$ ) and blanketing ( $f_bE_s$ ) frequencies, indicating the significant variability of electron density in horizontal space (Ogawa et al. 2002). Imaging observation of  $Mg^+$  resonance scatter from a sounding rocket also observed such horizontally patchy structures in the  $Mg^+$  densities, which suggest electron density irregularities in the  $E_s$  layer (Kurihara et al. 2010).

Recently, three-dimensional numerical modeling studies have suggested that plasma density irregularities in the  $E_s$  layer play a key role for seeding medium-scale traveling ionospheric disturbances (MSTIDs) in the  $F$  region through ionospheric  $E$  and  $F$  region coupling process (Yokoyama and Hysell 2010; Yokoyama 2013). However, generation mechanisms of the plasma density irregularities in the  $E_s$  layer are still under investigation. Because the plasma density in the  $E$ -region is about six orders smaller than the neutral density, the contribution of neutral wind dynamics to creating plasma irregular structures is significantly large. Gravity wave modulation of the  $E_s$  layer is proposed as one of the neutral drivers of these  $E$ -region plasma density irregularities (Woodman et al. 1991). Vertical shear of horizontal neutral wind may also drive  $E$ -region irregularities through the plane wave perturbations in the altitude or density imposed on the  $E_s$  layer (Cosgrove and Tsunoda 2003, 2004; Tsunoda and Cosgrove 2004), or the Kelvin–Helmholtz (K–H) instability that produces turbulence coupled to the plasma (Larsen 2000; Bernhardt 2002). The descriptions of the nonlinear evolution of these processes have been provided using numerical simulations (Cosgrove and Tsunoda 2003; Bernhardt 2002). However, spatial and temporal resolution for the  $E_s$  layer was not always sufficient in the IS radar and the resonance scattering lidar to determine the cause or evolution of  $E$ -region irregularities, though they have the capability to measure precise plasma height-time variations. Thus, the observed structures could not be compared with the results of the numerical model simulations and their causes and time evolution could not be adequately explored. For example, typical height and time resolution for the  $E_s$  layer observation by the Arecibo IS radar was 300 m and 10 s, respectively (e.g., Hysell et al. 2009) and by the  $Ca^+$  resonance scattering lidar was a few hundred meters and minutes (e.g., Gerding et al. 2000; Raizada et al. 2012).

In this study, the  $Ca^+$  resonance scattering lidar developed by the National Institute of Polar Research (NIPR) has measured  $Ca^+$  densities associated with the  $E_s$  layer

with a high height/time resolution of 15 m/5 s by taking advantage of the  $Ca^+_s$  layer, which has much higher  $Ca^+$  densities in comparison with the usual layer.

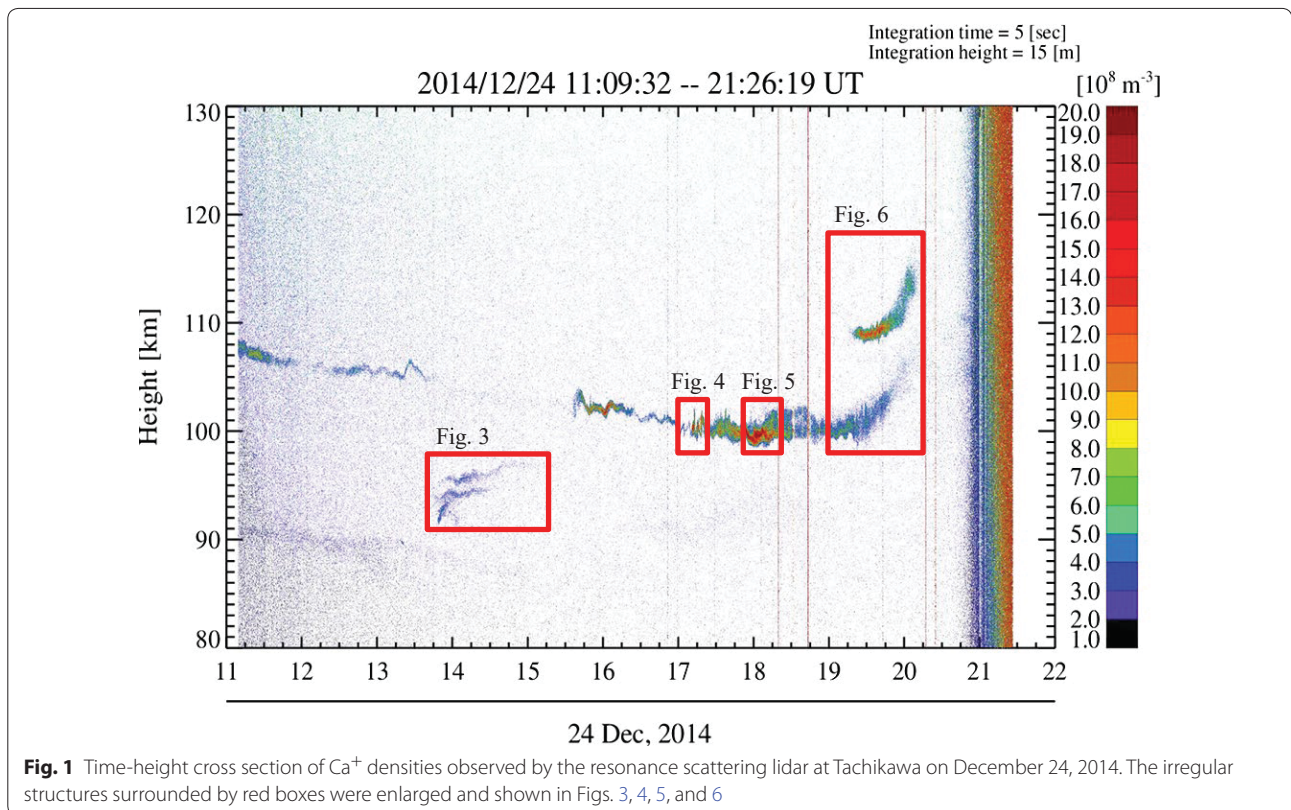
### Instrumentation

$Ca^+$  density profiles were measured using a frequency-tunable resonance scattering lidar at NIPR, Tachikawa (35.7°N, 139.4°E, 93 m height), from 11:09 to 21:26 UT on December 24, 2014. The lidar transmitter is based on an injection-seeded alexandrite ring laser for 768–788 nm (fundamental wavelengths) and a second harmonic generation (SHG) unit with two harmonic crystals (Barium Borate: BBO) for 384–394 nm (second harmonic wavelengths). The pulse width of the laser was 200–250 ns at a 25.0 Hz repetition rate, and the mean power was 0.2–0.3 W, where the wavelength was centered at 393.477 nm. A tunable diode laser (Toptica, DL pro 780) was used as a seed laser. The laser wavelengths were tuned to the resonance frequencies utilizing a wavelength meter (HighFines, WSU-10), which was calibrated using a wavelength-stabilized He–Ne laser. A Nasmyth-Cassegrain f/8 telescope with 83 cm diameter primary mirror was used as a receiver. Photons at 393.477 nm were detected by a Hamamatsu R9880U-210 (Ultra bialkali) photomultiplier tube (PMT) attached at the back of the telescope. A band-pass filter with a center wavelength of 389.7 nm, and an FWHM of 11.5 nm was used to reduce the background sky brightness. The photon counts were recorded by a transient recorder (Licel, PR10-160-P) with a range resolution of 15 m and integrated every 125 shots (5 s). Background noise (mean photon count: 200–230 km) was subtracted from the photon count profile, and the photon counts were normalized via the Rayleigh signal at 34–37 km to yield  $Ca^+$  densities. The minimum limit of determination was  $45 \text{ cm}^{-3}$ .

$E_s$  layer parameters were obtained by an ionosonde at Kokubunji (35.7°N, 139.5°E, 75 m height), located only ~7.5 km away from NIPR. The ionosonde is regularly operated by the National Institute of Information and Communications Technology (NICT). Ionograms were obtained by regular ionosonde observations every 15 min with a 15 s sweep time from 1 to 30 MHz. The field-of-view (FOV) of the ionosonde is several hundred km in diameter and covers the lidar FOV located at Tachikawa.  $E_s$  layers were detected intermittently throughout the night.

### Observation results and discussion

Figure 1 shows temporal variation of  $Ca^+$  density profiles observed between 11:09 and 21:26 UT on December 24, 2014. At the beginning of the observation, two sporadic  $Ca^+$  ( $Ca^+_s$ ) layers appeared at ~91 km and ~108 km. The upper layer was thin (<2 km) and descending with a

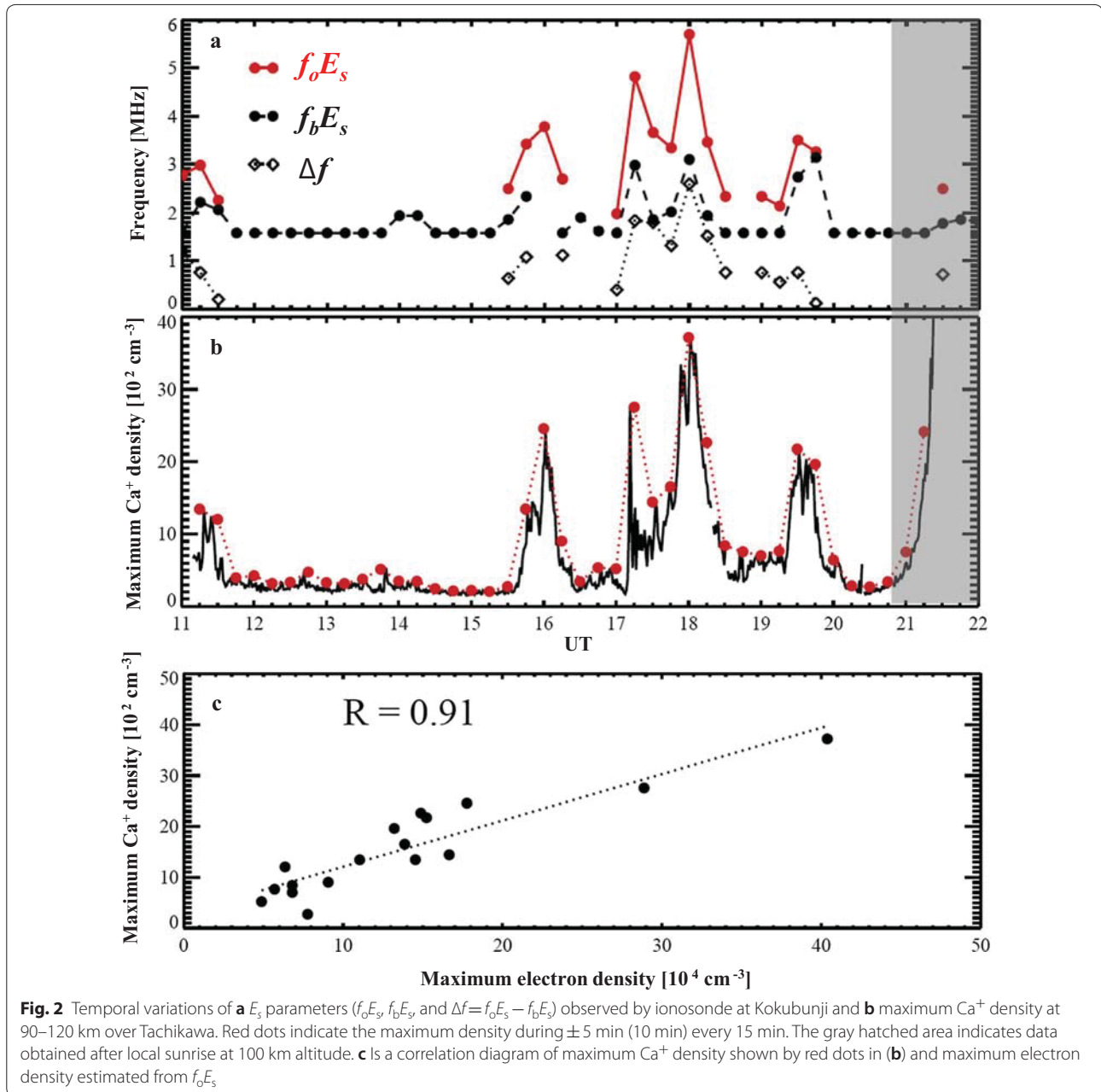


speed of  $\sim 1$  km/h (“main  $\text{Ca}^+$  layer” hereafter), while the lower layer was faint. These layers became unclear from 13:45–15:00 UT, until the other layers appeared between them ( $\sim 91$ – $97$  km). At 15:30–17:00 UT, the main  $\text{Ca}^+$  layer appeared again and descended to  $\sim 100$  km, while the lower layer could not be seen. After 17:00 UT, the main  $\text{Ca}^+$  layer was perturbed and showed some instability-like structures. The layer height did not change from  $\sim 100$  km, though the layer width grew larger. At 19:15–20:15 UT, which was just before local sunrise at 100 km, the main  $\text{Ca}^+$  layer moved upward. At the same time, another  $\text{Ca}^+$  layer appeared at 109 km and moved upward. After 20:45 UT, background noise increased due to sunrise at  $\sim 100$  km altitude.

The  $E_s$  layers were also observed intermittently by the ionosonde at Kokubunji. Observed  $E_s$  layer parameters, such as the critical frequency ( $f_oE_s$ , shown by red dots) and blanketing frequency ( $f_bE_s$ , shown by black dots), are displayed in Fig. 2a. The time after the sunrise at 100 km is demarcated by gray hatching.  $f_oE_s$  and  $f_bE_s$  both correspond to the maximum and minimum electron densities in the  $E_s$  layer, respectively. Therefore, a large difference ( $\Delta f$ ) between  $f_oE_s$  and  $f_bE_s$  means there is a large difference between the maximum and minimum electron densities within the field-of-view (FOV) of the ionosonde. During the times that the  $E_s$  layer ( $f_oE_s$ ) was observed by

the ionosonde (11:00–11:30 UT, 15:30–16:15 UT, 17:00–18:30 UT, and 19:00–19:45 UT), the  $\text{Ca}^+$  densities were relatively higher. Temporal variation of the maximum  $\text{Ca}^+$  densities at 90–120 km is shown in Fig. 2b where red dots indicate the maximum density in 10 min window, displayed every 15 min. Temporal variations of maximum  $\text{Ca}^+$  density and  $f_oE_s$  in Fig. 2a, b show that the  $f_oE_s$  was determined from the ionogram only when the maximum  $\text{Ca}^+$  densities were larger than approximately  $500 \text{ cm}^{-3}$ . The correlations between the maximum  $\text{Ca}^+$  densities and the maximum electron densities estimated from  $f_oE_s$ , are shown in Fig. 2c. They show a strong correlation with a coefficient of 0.91 where the maximum  $\text{Ca}^+$  density was two orders of magnitude smaller than the maximum electron density. These results suggest that  $\text{Ca}^+$  contributes forming the  $E_s$  layer as well as major metallic ions  $\text{Fe}^+$  and  $\text{Mg}^+$  in the lower thermosphere.

Characteristic wave-like and irregular structures surrounded by red boxes were seen in the  $\text{Ca}^+$  layers and were enlarged as shown in Figs. 3, 4, 5 and 6. Figure 3a shows wave-like structures observed at 91–97 km from 13:45 UT to  $\sim 15:00$  UT. The wave-like structures had three layers with a vertical distance of  $\sim 1.2$  km. The upper two layers fluctuated with an observed period of  $\sim 15$  min and moved upward with a speed of  $\sim 0.5$  m/s. Temporal variations of average  $\text{Ca}^+$  density



at 95–97 km, 93.5–95 km and 91–93.5 km are shown in Fig. 3b–d, respectively. Vertical dashed lines indicate the time when the densities were the maximum and horizontal dashed lines indicate  $e^{-1}$  values of the maximum densities.  $\text{Ca}^+$  density in the bottom layer became the maximum at first, followed by the middle and top layers with a time delay of  $\sim 9$  min each. Time interval from when the density maximized to when it decreased to  $e^{-1}$  ( $\tau_{\text{obs}}$ ) was 7 min, 23 min, and 30 min in the bottom, middle, and top layers, respectively. According to

Raizada et al. (2012), the lifetime ( $\tau_{\text{theo}}$ ) of  $\text{Ca}^+$  in the mesosphere and lower-thermosphere region increases with height, with lifetimes in winter at 91–93.5 km, 93.5–95 km, and 95–97 km are  $\sim 10$  min, 10–30 min, and 30–70 min, respectively. The observed time intervals from the peak to  $e^{-1}$  of densities that we identified were comparable but slightly shorter than the theoretical lifetimes. The wave-like structures may have been carried by background neutral wind. Meteoric ablation is a possible mechanism of the  $\text{Ca}^+$  generation

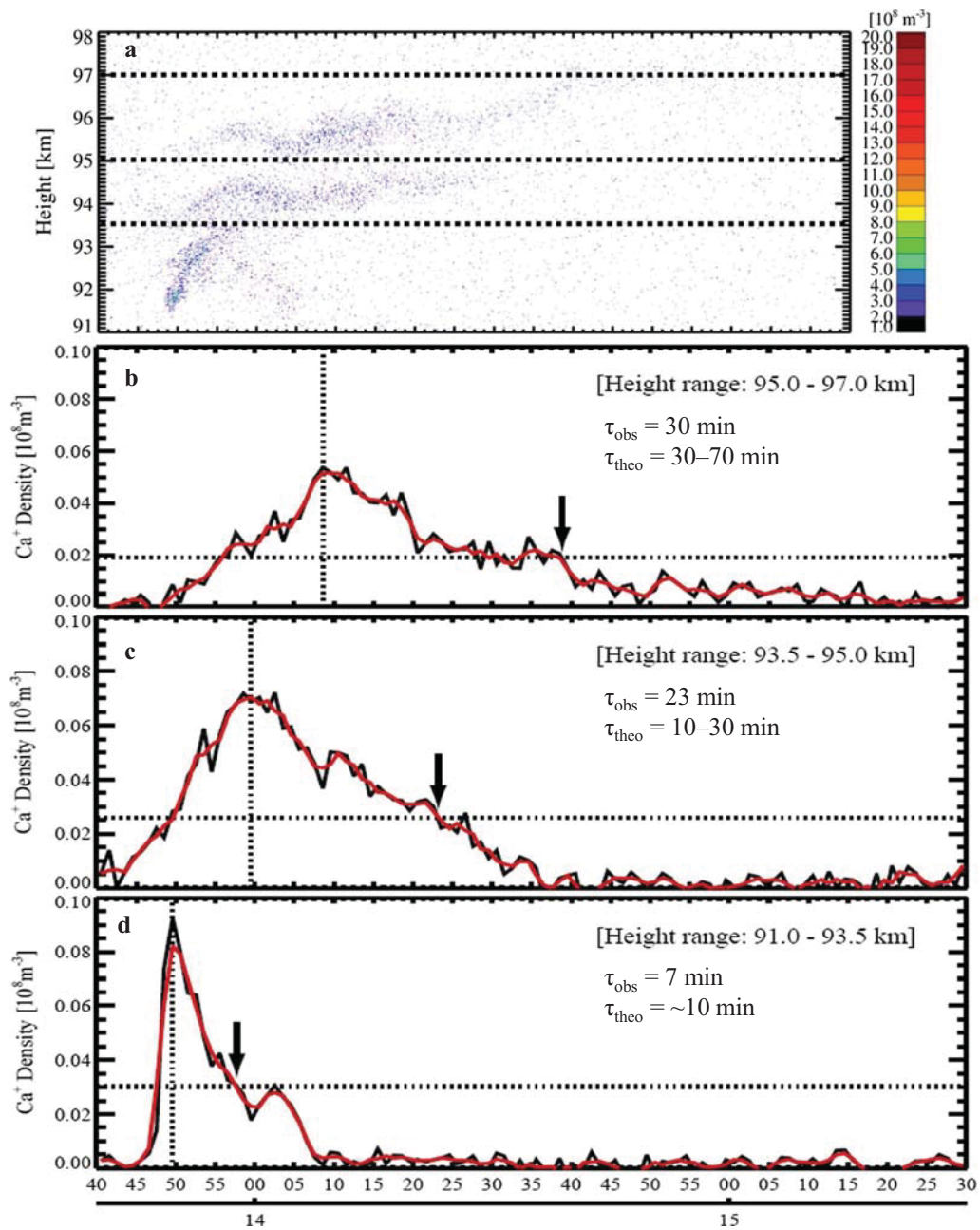


**Fig. 3** a Wave-like structures observed at 91–97 km from 13:45 UT to 15:00 UT. Ca<sup>+</sup> layers, which had a distance of approximately 1.2 km, fluctuated vertically with a period of ~15 min. They moved upward with a speed of ~0.5 m/s. Temporal variations of average Ca<sup>+</sup> density at **b** 95–97 km, **c** 93.5–95 km, and **d** 91–93.5 km. Vertical dashed lines indicate the time when the densities became the maximum and horizontal dashed lines indicate e<sup>-1</sup> values of the maximum densities. Black arrows indicate the time when average densities became smaller than e<sup>-1</sup> values

during the night. The Ca<sup>+</sup> density distribution showed three layers at 91–97 km. That could be caused by three times of strong meteoric ablations from a single meteor event, which is called the “blob” structure. The Ca<sup>+</sup> might be transported by background neutral wind into the FOV of our lidar observation, while it is diffusing

horizontally by the molecular diffusion and decreasing exponentially with the lifetime. In order to understand the mechanism of Ca<sup>+</sup> generation, the formation of the layer structure, and the causes of the fluctuation, background wind measurements with high time and height resolutions are required.

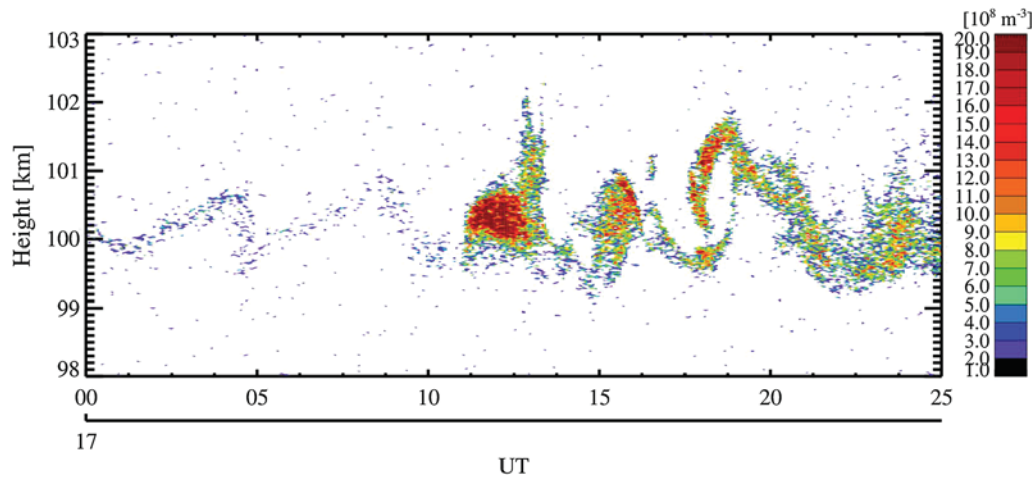


**Fig. 4** Instability-like structures were observed at around 100 km. A “cats-eye” structure that is suggestive of large-scale deformation by neutral dynamical (Kelvin–Helmholtz) instability is clearly seen at 99.5–102 km at 17:17–17:19 UT

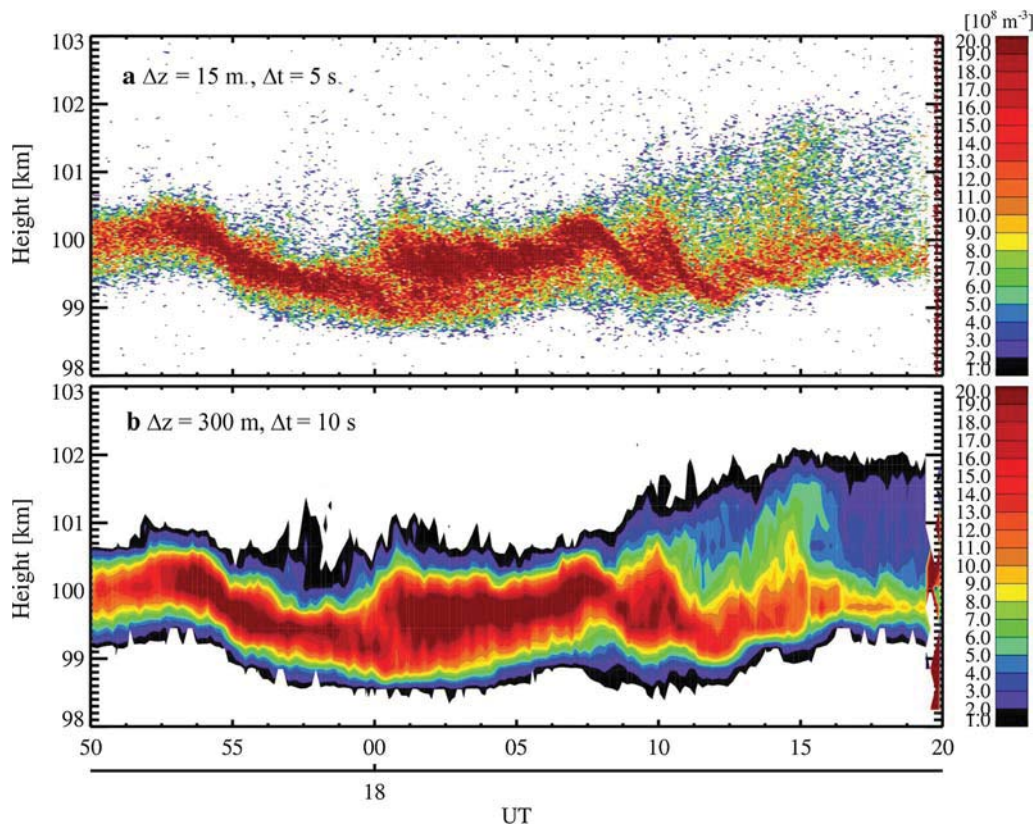
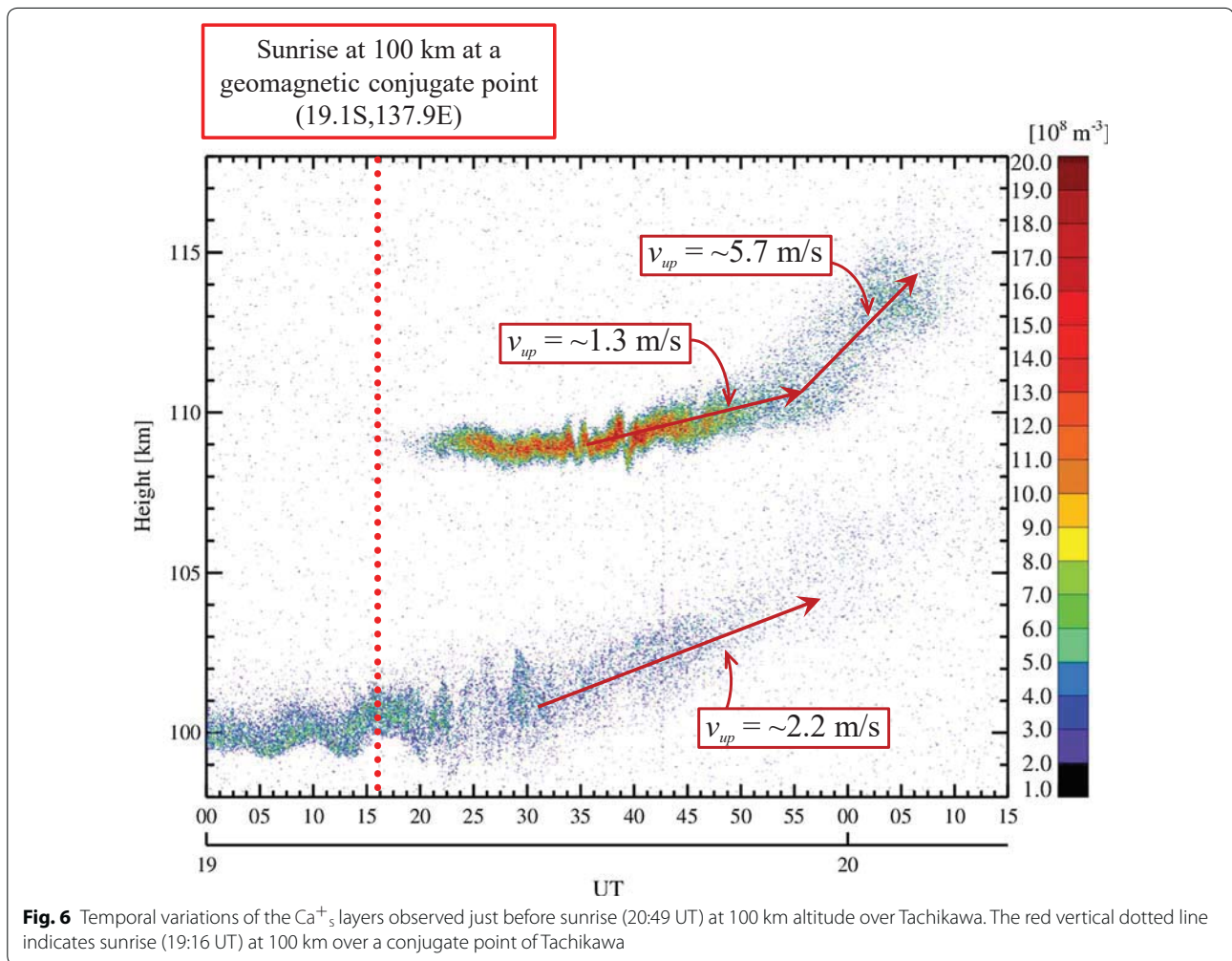


**Fig. 5** Time evolution of instability structures in the  $\text{Ca}^+$  layer at  $\sim 100$  km is displayed with height and time integrations of 15 m and 5 s (a) and of 300 m and 10 s (b). The high height-time resolution observation (b) reveals detailed structures of the K–H instability in the  $\text{Ca}^+$  layer

The  $\text{Ca}^+$  layer at around 100–101 km (Fig. 4) showed a vertical displacement seen as a quasi-sinusoidal variation with an observed period of  $\sim 5$  min from 17:00 to

17:11 UT. Following this variation, a localized-clump of  $\text{Ca}^+$  was formed repeatedly with an interval of  $\sim 2.5$  min. At 17:17–17:19 UT, a “cats-eye” feature, suggesting a



large-scale deformation due to K–H instability, was clearly seen at 99.5–102 km. The quasi-sinusoidal variation and irregular structures are likely structures in the ionospheric ion layers that were formed in response to turbulence in the neutral atmosphere. According to a two-dimensional numerical model simulation by Bernhardt (2002), nonlinear evolution of ion layers in the lower thermosphere in response to turbulence due to the neutral wind shear depends on a ratio of ion-neutral collision frequency ( $\nu_i$ ) to ion gyrofrequency ( $\omega_i$ ). At 100 km altitude, the  $\nu_i$  is larger than the  $\omega_i$ , and therefore the neutral wind shear generates compression and twisting of the  $E_s$  layer densities and then ultimately yields two modulated layers of electron density through the K–H instability structures (“cats-eye”). The localized clumps are formed where the  $\omega_i$  is nearly equal to the  $\nu_i$ , such as at 120 km. The observed results with the localized clumps just before the formation of the “cats-eye” structure at ~100 km means the neutral density in the background was temporarily or spatially smaller than usual.

In Fig. 5a, twisted structures in the Ca<sup>+</sup><sub>s</sub> layer, probably caused by the K–H instability, were clearly seen between 18:00 and 18:10 UT. The maximum Ca<sup>+</sup> density in the Ca<sup>+</sup><sub>s</sub> layer increased in time, followed by the twisting of the Ca<sup>+</sup><sub>s</sub> layer at around 18:00 UT. The twisted structure then developed a K–H billow at around 18:10 UT. After 18:12 UT, the K–H billow disappeared, and the layer thickness became broader from 2 to 3 km. As shown in Fig. 1, this layer was then split into two modulated layers with a separation of about 2 km at ~18:30 UT. The observed time evolution of ion layer modulation agreed with the results of numerical model simulation at ~100 km (Bernhardt 2002). The upper layer (~102 km altitude) descended after ~18:40 UT and merged into a single layer at ~18:50 UT as seen in Fig. 1. To demonstrate the capability of high time and height resolution (5 s, 15 m) by our lidar, the same  $E_s$  layer observation was plotted with a resolution of the 300 m and 10 s integrations, which were used as typical resolutions for the



Arecibo radar observation, in Fig. 5b. Temporal variations of the maximum  $\text{Ca}^+$  density and the  $\text{Ca}^+_{\text{s}}$  layer thickness can be obtained, however, to reveal the detailed structures such as the twist in the  $\text{Ca}^+_{\text{s}}$  density requires higher height-time resolution.

Figure 6 shows temporal variations of the  $\text{Ca}^+_{\text{s}}$  layers observed just before local sunrise. The main  $\text{Ca}^+_{\text{s}}$  layer at  $\sim 100$  km exhibited quasi-periodic vertical oscillation with a wave period of 8 min until 19:20 UT. Then, the amplitude of oscillation became larger. The layer width gradually increased between 19:00 and 19:30 from 1 to 3 km. After 19:30 UT, the oscillation was unclear but upward motion of the layer became obvious, with a speed of  $\sim 2.2$  m/s. Together with the upward motion, the layer was faded out after 19:50 UT. Another  $\text{Ca}^+_{\text{s}}$  layer appeared at around 19:20 UT at 109 km. This layer started to oscillate with a period of  $\sim 3$  min at around 19:33 UT, moved upward at a rate of  $\sim 1.3$  m/s after 19:35 UT, and then started to diffuse vertically at 19:45 UT. The upward speed increased to  $\sim 5.7$  m/s after 19:55 UT. The sunrise time at 100 km altitude over Tachikawa was 20:49 UT, while the sunrise at the geomagnetic conjugate to Tachikawa was 19:16 UT (red dotted line in Fig. 6). In short, those, the main  $\text{Ca}^+_{\text{s}}$  layer started diffuse, a new  $\text{Ca}^+_{\text{s}}$  layer emerged, and both layers moved upward, were observed after the sunrise at the conjugate point but before the sunrise at Tachikawa.

In the lower thermosphere,  $\text{Ca}^+$  plays as a tracer of neutral atmospheric dynamics. However, it is well accepted that mean vertical wind is quite small ( $\sim 0$  m/s) in the mid-latitude and such upward flow is unlikely to continue more than 30 min. On the other hand, when  $\text{Ca}^+$  behaves as plasma in the  $E_{\text{s}}$  layer, the ion velocity ( $\vec{v}$ ) can be expressed by (Cosgrove and Tsunoda 2002)

$$\vec{v} = \frac{\rho_i}{1 + \rho_i^2} \left( \frac{\vec{E}_{\perp}}{B} + \vec{u} \times \hat{b} \right) + \frac{1}{1 + \rho_i^2} \left( \frac{\vec{E}_{\perp}}{B} + \vec{u} \times \hat{b} \right) \times \hat{b} + \vec{u} \quad (1)$$

Here  $\vec{B} = B\hat{b}$  is the magnetic field,  $\vec{E}_{\perp}$  is the electric field perpendicular to  $\vec{B}$ , and the electric field parallel to  $\vec{B}$  has been set to zero.  $\vec{u}$  is the background neutral wind velocity.  $\rho_i$  is the ratio of the ion-neutral collision frequency ( $\nu_i$ ) to the ion gyrofrequency ( $\omega_i$ ). Calculating the ion-neutral collision frequency, which was obtained from Banks and Kockarts (1973), using densities of the nitrogen and oxygen molecules and the nitrogen atoms, calculated by NRLMSISE-00 (Picone et al. 2002),  $\rho_i$  over Tachikawa is 34.2 at 100 km and 5.2 at 110 km. To move the ion upward, eastward wind ( $\vec{u}_{\text{E}}$ ) in the first term or eastward electric field ( $\vec{E}_{\text{E}}$ ) in the second term

is required. The last term has no contribution to vertical motion. Here, we assume that the upward motion is solely caused by the eastward electric field. The neutral wind is assumed to be zero. In that case, ion upward velocity ( $\vec{v}_{\text{up}}$ ) may be written as:

$$\vec{v}_{\text{up}} = \vec{v}_{\perp} \cdot \cos I = \frac{1}{1 + \rho_i^2} \cdot \left( \frac{\vec{E}_{\text{E}} \times \hat{b}}{B} \right) \cdot \cos I \quad (2)$$

where  $\vec{v}_{\perp}$  is the ion velocity perpendicular to  $\vec{B}$ . According to the IGRF-12 (International Geomagnetic Reference Field) model (Thebault et al. 2015), the geomagnetic inclination ( $I$ ) and total magnetic field intensity ( $B$ ) are derived to be  $49.5^\circ$  and  $44,350$  nT. When  $v_{\text{up}}$  is 2.2 m/s at 100 km and 1.3 m/s and 5.7 m/s at 110 km, required  $E_{\text{E}}$  is 176 mV/m, 2.5 mV/m, and 11 mV/m, respectively. These are quite large values in comparison with the eastward electric field ( $< 1$  mV/m) observed at the sunrise time at Jicamarca in the equatorial region as the pre-reversal enhancement (Kelley et al. 2014). It is difficult to explain that observed upward drift of  $\text{Ca}^+_{\text{s}}$  is due to only the  $\vec{E} \times \vec{B}$  drift driven by the eastward electric field generated by sunrise at the conjugate point ( $19.1^\circ\text{S}$ ,  $137.9^\circ\text{E}$ ). On the other hand, assuming that the upward motion is solely caused by the eastward neutral wind, without polarization field ( $\vec{E} = 0$ ),  $\vec{v}_{\text{up}}$  may be written as:

$$\vec{v}_{\text{up}} = \vec{v}_{\perp} \cdot \cos I = \frac{\rho_i}{1 + \rho_i^2} \cdot \left( \vec{u}_{\text{E}} \times \hat{b} \right) \cdot \cos I \quad (3)$$

Again, when  $v_{\text{up}}$  is at 100 km and 1.3 m/s and 5.7 m/s at 110 km, it is required that  $\vec{u}_{\text{E}}$  is 116 m/s, 11 m/s, and 47 m/s, respectively. Eastward wind of 116 m/s is relatively fast but possible where maximum wind speed often exceeds 100 m/s in the lower thermosphere (e.g., Larsen 2002). If strong eastward wind occurs near 100 km, the new  $\text{Ca}^+_{\text{s}}$  layer could be formed above the wind maximum by a vertical shear generated by the strong eastward wind. Therefore, an occurrence of strong eastward wind around 100 km was a possible cause of the observed phenomena. In addition, the upward movement of the wind shear structure, occurring ion convergence, also could be a reason of the observed upward movement of  $\text{Ca}^+$  layer. If the wind share structure with some angles passes through the FOV of the lidar, observed height of the  $\text{Ca}^+_{\text{s}}$  layer ascends/descends with time. Although these scenarios cannot be confirmed thoroughly without wind measurement, the observed phenomena were likely to be caused by strong horizontal winds, rather than the enhancement of the eastward electric field. However, the presence or absence of a causal relationship with the sunrise at the conjugate point is not clear.

## Summary

Vertical fine structures and the time evolution of plasma irregularities in the  $E_s$  layer have been observed via  $\text{Ca}^+$  density measurements using a resonance scattering lidar at Tachikawa (35.7°N, 139.4°E) on December 24, 2014, with a high time-height resolution of 5 s and 15 m. The  $\text{Ca}^+_{s}$  layer height at around 100 km showed quasi-sinusoidal variation at around 17:00 UT. Following this variation, the  $\text{Ca}^+$  formed localized clumps and the “cats-eye” structure was generated. Time evolution of twist structures was clearly observed in the  $\text{Ca}^+_{s}$  layer at around 18:00 UT. The fine structures of such plasma irregularities suggested that the K–H instabilities occurred in the neutral atmosphere whose density changed temporarily or spatially. The maximum  $\text{Ca}^+$  density in the  $\text{Ca}^+_{s}$  layer was two orders of magnitude smaller than the maximum electron density estimated from the  $f_oE_s$  observed by the ionosonde at Kokubunji (35.7°N, 139.5°E), located only ~7.5 km away from NIPR, simultaneously. The correlation showed a strong positive correlation with a coefficient of 0.91. These results suggest that  $\text{Ca}^+$  contributes forming the  $E_s$  layer as well as major metallic ions  $\text{Fe}^+$  and  $\text{Mg}^+$  in the lower thermosphere. The formation of a new  $\text{Ca}^+_{s}$  layer at 110 km altitude and the upward motion of the  $\text{Ca}^+_{s}$  layers at 100 km and 110 km were observed just after the sunrise time at the conjugate point and before the local sunrise. A possible explanation for the observed phenomena was the occurrence of strong horizontal wind, rather than the enhancement of the eastward electric field. The presence or absence of a causal relationship with the sunrise at the conjugation point and Tachikawa is still an open question.

## Abbreviations

$E_s$ : sporadic E;  $\text{Ca}^+_{s}$ : sporadic  $\text{Ca}^+$ ; K–H: Kelvin–Helmholtz; NIPR: National Institute of Polar Research.

## Authors' contributions

MKE (corr-auth) was involved in lidar development and observation and discussion. TN contributed to lidar development and observation and discussion. TT contributed to lidar development and observation. TN helped in lidar development and observation and discussion. MA was involved in lidar development. TT helped in lidar observation and discussion. KT contributed to Lidar development and observation. TDK was involved in Lidar development. TO helped in Lidar development. SW contributed to Lidar development. All authors read and approved the final manuscript.

## Author details

<sup>1</sup> National Institute of Polar Research, 10-3, Midoricho, Tachikawa, Tokyo 190-8518, Japan. <sup>2</sup> Department of Polar Science, SOKENDAI (The Graduate University for Advanced Studies), 10-3, Midoricho, Tachikawa, Tokyo 190-8518, Japan. <sup>3</sup> The University of Electro-Communications, 1-5-1, Chofugaoka, Chofu, Tokyo 182-8585, Japan. <sup>4</sup> Tokyo Metropolitan University, 6-6, Asahigaoka, Hino, Tokyo 191-0065, Japan. <sup>5</sup> RIKEN, RAP, 2-1, Hirosawa, Wako, Saitama 351-0198, Japan. <sup>6</sup> Faculty of Engineering, Shinshu University, 4-17-1, Wakasato, Nagano 380-8553, Japan.

## Acknowledgements

This work was supported by the JSPS-Kakenhi (JP15K13575), the prioritized project AJ1 and AJ0901 of Japanese Antarctic Research Expedition, and the Project Research KP2 and KP301 of the National Institute of Polar Research. The lidar data can be accessed at: <http://id.nii.ac.jp/1291/00014958/>. Ionosonde data at Kokubunji were provided by the World Data Center for Ionosphere through the National Institute of Information and Communications Technology, Tokyo. The preparation of this paper was supported by an NIPR publication subsidy.

## Competing interests

The authors declare that they have no competing interests.

## Availability of data and materials

The lidar data can be accessed at: <http://id.nii.ac.jp/1291/00014958/>. Ionosonde data at Kokubunji were provided by the World Data Center for Ionosphere through the National Institute of Information and Communications Technology, Tokyo.

## Consent for publication

Not applicable.

## Ethics approval and consent to participate

Not applicable.

## Funding

The JSPS-Kakenhi (JP15K13575), the prioritized project AJ1 and AJ0901 of Japanese Antarctic Research Expedition, the Project Research KP2 and KP301 of the National Institute of Polar Research. NIPR publication subsidy

## Publisher's Note

Springer Nature remains neutral with regard to jurisdictional claims in published maps and institutional affiliations.

Received: 12 September 2018 Accepted: 2 January 2019

Published online: 11 January 2019

## References

- Banks PM, Kockarts G (1973) *Aeronomy part A*. Academic Press, New York, pp 184–239
- Bernhardt PA (2002) The modulation of sporadic-E layers by Kelvin–Helmholtz billows in the neutral atmosphere. *J Atmos Solar Terr Phys* 54:1487–1504. [https://doi.org/10.1016/S1364-6826\(02\)00086-X](https://doi.org/10.1016/S1364-6826(02)00086-X)
- Cosgrove RB, Tsunoda RT (2002) A direction-dependent instability of sporadic-E layers in the nighttime midlatitude ionosphere. *Geophys. Res. Lett.* 29:1864. <https://doi.org/10.1029/2002GL014669>
- Cosgrove RB, Tsunoda RT (2003) Simulation of the nonlinear evolution of the sporadic-E layer instability in the nighttime midlatitude ionosphere. *J Geophys Res* 108:1283. <https://doi.org/10.1029/2002JA009728>
- Cosgrove RB, Tsunoda RT (2004) Instability of the E–F coupled nighttime midlatitude ionosphere. *J Geophys Res* 109:A04305. <https://doi.org/10.1029/2003JA010243>
- Gerding M, Alpers M, von Zahn U, Rollason RJ, Plane JMC (2000) The atmospheric Ca and  $\text{Ca}^+$  layers: midlatitude observations and modeling. *J Geophys Res* 105:27131–27146. <https://doi.org/10.1029/2000JA900088>
- Haldoupis C (2012) Midlatitude sporadic E. A typical paradigm of atmosphere-ionosphere coupling. *Space Sci Rev* 168:441–461. <https://doi.org/10.1007/s11214-011-9786-8>
- Hysell DL, Nossa E, Larsen MF, Munro J, Sulzer MP, Gonza'lez SA (2009) Sporadic E layer observations over Arecibo using coherent and incoherent scatter radar: assessing dynamic stability in the lower thermosphere. *J Geophys Res* 114:A12303. <https://doi.org/10.1029/2009JA014403>
- Kelley MC, Rodrigues FS, Pfaff RF, Klenzing J (2014) Observations of the generation of eastward equatorial electric fields near dawn. *Ann Geophys* 32:1169–1175. <https://doi.org/10.5194/angeo-32-1169-2014>
- Kurihara J, Koizumi-Kurihara Y, Iwagami N, Suzuki T, Kumamoto A, Ono T, Nakamura M, Ishii M, Matsuoka A, Ishisaka K, Abe T, Nozawa S (2010) Horizontal structure of sporadic E layer observed with a rocket-borne magnesium

- ion imager. *J Geophys Res* 115:A12318. <https://doi.org/10.1029/2009JA014926>
- Larsen MF (2000) A shear instability seeding mechanism for quasiperiodic radar echoes. *J Geophys Res* 105:24931–24940. <https://doi.org/10.1029/1999JA000290>
- Larsen MF (2002) Winds and shears in the mesosphere and lower thermosphere: results from four decades of chemical release wind measurements. *J Geophys Res* 107(A8):1215. <https://doi.org/10.1029/2001JA000218>
- MacLeod MA (1966) Sporadic E theory: I. Collision-geomagnetic equilibrium. *J Atmos Sci* 23:96–109. [https://doi.org/10.1175/1520-0469\(1966\)023%3c0096:SETICG%3e2.0.CO;2](https://doi.org/10.1175/1520-0469(1966)023%3c0096:SETICG%3e2.0.CO;2)
- Mathews JD (1998) Sporadic E: current views and recent progress. *J Atmos Solar Terr Phys* 60:413–435. [https://doi.org/10.1016/S1364-6826\(97\)00043-6](https://doi.org/10.1016/S1364-6826(97)00043-6)
- Ogawa T, Takahashi O, Otsuka Y, Nozaki K, Yamamoto M, Kita K (2002) Simultaneous middle and upper atmosphere radar and ionospheric sounder observations of midlatitude E region irregularities and sporadic E layer. *J Geophys Res* 107(A10):1275. <https://doi.org/10.1029/2001JA900176>
- Picone JM, Hedin AE, Drob DP (2002) NRLMSISE-00 empirical model of the atmosphere: statistical comparisons and scientific issues. *J Geophys Res* 107(A12):1468. <https://doi.org/10.1029/2002JA009430>
- Raizada S, Tepley CA, Williams BP, Garcia R (2012) Summer to winter variability in mesospheric calcium ion distribution and its dependence on sporadic E at Arecibo. *J Geophys Res* 117:A02303. <https://doi.org/10.1029/2011JA016953>
- Thebault E, Finlay CC, Beggan CD, Alken P, Aubert J, Barrois O, Bertrand F, Bondar T, Boness A, Brocco L, Canet E, Chambodut A, Chulliat A, Coisson P, Civet F, Du A, Fournier A, Fratter I, Gillet N, Hamilton B, Hamoudi M, Hulot G, Jager T, Korte M, Kuang W, Lalanne X, Langlais B, Leger J-M, Lesur V, Lowes FJ, Macmillan S, Mandaia M, Manoj C, Maus S, Olsen N, Petrov V, Ridley V, Rother M, Sabaka TJ, Saturnino D, Schachtschneider R, Sirol O, Tangborn A, Thomson A, Toffner-Clausen L, Vigneron P, Wardinski I, Zvereva T (2015) International geomagnetic reference field: the 12th generation. *Earth Planets Space*. <https://doi.org/10.1186/s40623-015-0228-9>
- Tsunoda RT, Cosgrove RB (2004) Azimuth-dependent  $E_s$  layer instability: a missing link found. *J Geophys Res* 109:A12303. <https://doi.org/10.1029/2004>
- Whitehead JD (1961) The formation of the sporadic-E layer in the temperate zone. *J Atmos Terr Phys* 20:49–58. [https://doi.org/10.1016/0021-9169\(61\)90097-6](https://doi.org/10.1016/0021-9169(61)90097-6)
- Whitehead JD (1970) Production and prediction of sporadic E. *Rev Geophys* 8:65–144. <https://doi.org/10.1029/RG008i001p00065>
- Whitehead JD (1989) Recent work on mid-latitude and equatorial sporadic E. *J Atmos Terr Phys* 51:401–424. [https://doi.org/10.1016/0021-9169\(89\)90122-0](https://doi.org/10.1016/0021-9169(89)90122-0)
- Woodman RF, Yamamoto M, Fukao S (1991) Gravity wave modulation of gradient drift instabilities in mid-latitude sporadic E irregularities. *Geophys Res Lett* 18(1197):1200. <https://doi.org/10.1029/91GL01159>
- Yamamoto M, Fukao S, Woodman RF, Ogawa T, Tsuda T, Kato S (1991) Mid-latitude E region field-aligned irregularities observed with the MU radar. *J Geophys Res* 96:15943–15949
- Yamamoto M, Fukao S, Ogawa T, Tsuda T, Kato S (1992) A morphological study on midlatitude E-region field-aligned irregularities observed with the MU radar. *J Atmos Solar Terr Phys* 54:769–777. [https://doi.org/10.1016/0021-9169\(92\)90115-2](https://doi.org/10.1016/0021-9169(92)90115-2)
- Yokoyama T (2013) Scale dependence and frontal formation of nighttime medium-scale traveling ionospheric disturbances. *Geophys Res Lett* 40:4515–4519. <https://doi.org/10.1002/grl.50905>
- Yokoyama T, Hysell DL (2010) A new midlatitude ionosphere electrodynamics coupling model (MIECO): latitudinal dependence and propagation of medium-scale traveling ionospheric disturbances. *Geophys Res Lett* 37:L08105. <https://doi.org/10.1029/2010GL042598>

Submit your manuscript to a SpringerOpen<sup>®</sup> journal and benefit from:

- Convenient online submission
- Rigorous peer review
- Open access: articles freely available online
- High visibility within the field
- Retaining the copyright to your article

---

Submit your next manuscript at ► [springeropen.com](https://www.springeropen.com)

---